Mapping global impervious surface area and green space within urban environments

Wenhui KUANG[*]

Key Laboratory of Land Surface Pattern and Simulation, Institute of Geographic Sciences and Natural Resources Research, Chinese Academy of Sciences, Beijing 100101, China

Abstract   The mapping of impervious surface area (ISA) and urban green space (UGS) is essential for improving the urban environmental quality toward ecological, livable, and sustainable goals. Currently, accurate ISA and UGS products are lacking in urban areas at the global scale. This study established regression models that estimated the fraction of ISA/UGS in global 30 cities for validation using MODIS NDVI and DMSP/OLS nighttime light imageries. A global dataset of ISA and UGS fraction with a spatial resolution of 250 m×250 m was developed using the regression model, with a mean relative error of 0.19 for its ISA. The results showed the global urban area of 76.29×10^4 km^2, which was primarily distributed in central Europe, eastern Asia, and central and eastern North America. The urban land area in North America, Europe, and Asia was 66.3×10^4 km^2, accounting for 86.91% of the world's urban area; the urban land area of the top 50 countries accounted for 59.32% of the total urban land area in the world. The global ISA of 45.26×10^4 km^2 was mainly distributed in central and southern North America, eastern Asia, and Europe, as well as coastal regions around the world. The proportion of ISA situated in built-up areas on the continental scale followed the order of Africa (>70%)>South America>Oceania>Asia (>60%)>North America>Europe (>50%), and these areas were mostly in southeastern North America, southwestern Europe, and eastern and western Asia. North America, Europe, and Asia accounted for 89.44% of the world's total UGS. The cities of developed countries in Europe and North America exposed a dramatic mosaic of ISA and UGS composites in urban construction. Therefore, the proportion of UGS is relatively high in those cities. However, in developing and underdeveloped countries, the proportion of UGS in built-up areas is relatively low, and urban environments need to be improved for livability.

Keywords   Impervious surface area, Green space, Habitat environment, Remote sensing classification, Global scale

1. Introduction

Global warming and rapid urbanization have serious impacts on urban environments, ecosystem services, and human well-being (Grimm et al., 2008; Creutzig et al., 2016). The core themes of the Intergovernmental Panel on Climate Change (IPCC) became the promotion of ecological resilience and adaptability to climate change in cities and communities and the establishment of comfortable and sustainable cities (Georgescu et al., 2014; Sanchez Rodriguez et al., 2018). The growth of metropolitan cities has resulted in the intensifying frequency of extreme heat events. It has been predicted that people in cities could be increasingly exposed to extreme heat waves in the future (Bierwagen et al., 2010; Georgescu et al., 2013; Jones et al., 2015). Rapid urbanization has resulted in a series of ecological and environmental issues, such as the ceaseless expansion of man-made surfaces, the aggravation of urban heat islands, the rise of regional air temperatures, and the decline in urban ecosystem services (Chen et al., 2016; Fang et al., 2017).

* Corresponding author (email: kuangwh@igsnrr.ac.cn)

As indicators of urbanization, impervious surface area (ISA) and urban green space (UGS) play important roles in assessing the health of urban ecosystems and the quality of human settlements (Lee et al., 2018). ISA includes building roofs, roads, squares, airports, and other impervious surfaces, all of which are covered by materials such as asphalt, concrete, brick, and stone. UGS is mainly different types of urban greening, i.e., parks, forests, and grasslands within built-up areas. ISA, UGS, waterbodies, and bare soil make up urban land-cover types (Kuang et al., 2016a). Urban land is internally characterized by high heterogeneity of spatial patterns, complex structures, component mosaics, and transformations between land cover types. Due to the differences in natural geography, economic and cultural factors, and planning modes within individual countries, the mosaicked modes of ISA and UGS composites vary remarkably among countries around the world. Therefore, remotely sensed classification and mapping of urban underlying surface cover at a global scale exist still two challenges: (1) developing an appropriate approach to retrieve ISA and UGS in different regions and (2) understanding the impacts of the mixed pixel problem on remotely sensed data. The acquisition of ISA and UGS fractions from coarse spatial resolution images is especially challenging.

Currently, ISA and UGS fraction mapping focus mainly on the classification of an ISA or UGS pixel at a national or regional scale. The United States Geological Survey (USGS) developed ISA fraction maps for its 2001, 2006, and 2011 National Land Cover Database (NLCD) with a resolution of 30 m×30 m (Homer et al., 2012), providing an important dataset for monitoring urban ecological and environmental quality (Yang et al., 2003; Wickham et al., 2013). Kuang et al. (2013) calculated the human settlement index (HSI) and analyzed the spatiotemporal patterns of the national ISA from 2000 to 2008, which derived from China's Land Use/ Cover Dataset (CLUD), nighttime light data (e.g., Defense Meteorological Satellites Program-Operational Linescan System (DMSP/OLS)), and Moderate Resolution Imaging Spectroradiometer (MODIS) normalized difference vegetation index (NDVI) data. In recent years, the development of modeling algorithms for extracting ISA, UGS, and other land cover types has considerably enhanced the monitoring capacity in urban ecology and the environment. With the increased availability of remote sensing images with high spatial resolution and improvements to mapping algorithms, the capacity for monitoring urban surfaces has remarkably improved at regional and city scales. The V-I-S model developed by Ridd (1995) decomposed urban land cover into vegetation (V), impervious surfaces (I), and soil (S). Subsequent studies extracted the ISA and UGS components in subpixels on the basis of linear spectral unmixing models using Landsat images (Wu and Murray, 2003; Lu and Weng, 2006; Lu et al., 2011; Li et al., 2016). Zhang and Weng

(2016) extracted urban ISA in the Pearl River basin between 1998 and 2013. Yue et al. (2006), Pan et al. (2009), and Li et al. (2016) also studied the distribution of urban land cover in Fuzhou, Lanzhou, and Hangzhou, respectively. These studies mainly focused on the mapping and spatiotemporal analysis of ISA distribution in specific cities. Some studies have compared the divergences in urban functions and structure associated with ISA and UGS in countries with different social conditions. Yu et al. (2017) monitored spatial expansion and conducted a comparative analysis in megacities along the Maritime Silk Road. The urban expansion in the Beijing-Tianjin-Hebei urban agglomeration in China was compared to that in the BosWash (Boston-Washington, D.C.) urban agglomeration in the USA (Cao et al., 2017).The intra-urban structures and their ISA percentages in the megacities of Beijing, Shanghai, and Guangzhou in China and New York, Chicago, and Los Angeles in the USA was also compared (Chi et al., 2015; Kuang et al., 2014). A new trend is emerging to guide urban planners for other countries through adopting from the prior knowledge of developed countries to improve urban ecosystem services.

At the global scale, the mapping of built-up areas, urban land, or ISA at resolutions of 1 km or 500 m is becoming a popular research topic. For example, Elvidge et al. (2007, 2010) developed a global dataset on constructed ISA with a resolution of 1 km using DMSP/OLS images, indicating a total area of constructed ISA of 57.97×10^4 km^2, accounting for approximately 0.43% of the world's land area in 2000/ 2001. Schneider et al. (2009, 2010) mapped urban areas at a resolution of 500 m using MODIS images with an overall accuracy of 93%. Liu et al. (2018) developed the normalized urban areas composite index (NUACI) to calculate the global urban area at 5-year intervals from 1990 to 2010 using the Google Earth Engine (GEE) cloud-computing platform. Their study estimated that the global urban area increased from $(45.10 \pm 0.12) \times 10^4$ km^2 in 1990 to $(74.71 \pm 0.15) \times 10^4$ km^2 in 2010, accounting for 0.63% of the world's total land area. Liu et al. (2014) noted the great divergences in previous research findings due to different definitions and data sources. They summarized that the world's built-up area accounts for approximately 0.65% of the global land area, with ISA covering 0.45% of total land area. Due to the high spatial heterogeneity of urban landscapes, ISA and UGS were usually mosaicked at the pixel level in 30-m resolution Landsat TM imagery. Therefore, previous studies that regarded ISA as a homogeneous unit at resolutions of 1 km or 500 m lacked effective decomposition for ISA and UGS in each pixel of the city. This condition limited the capacity of these studies to delineate urban structures and surface characteristics, as well as causing serious issues in mapping accuracy and data analysis. ISA and UGS have very different effects on surface radiation and the energy budget and in biogeophysical and biogeochemical processes. Conse-

quently, spatial resolution and accuracy of dataset in urban land mapping could play an important role on the evaluation of urban environments, carbon emission, and climate change.

In this study, we proposed a new hierarchical classification system and a mixed-pixel-based decomposition method that integrates multisource data and geo-knowledge rules to accurately delineate urban land cover (Kuang et al., 2016a; Zhuo et al., 2018). We developed a global ISA and UGS dataset using an integrated classification method from MODIS NDVI, DMSP/OLS and Landsat TM data using GlobeLand30 dataset (Chen et al., 2015). We examined the spatial heterogeneity of ISA and UGS among continents, countries, and cities and analyzed the relationships between urban greening and dweller habitat environments. This research will provide scientific knowledge related to the climate and ecological effects of urbanization, the assessment of the health status of urban habitat environments, and the evaluation of global ecosystem services and human well-being in cities.

2. Data and methods

2.1 Study area

The total area of global urban land is 76.29×10^4 km^2, accounting for 0.51% of the global land (Figure 1). The global population was 7.38 billion in 2015, with a population density of 49 people/km^2. Six continents-Asia (48 countries), Europe (43 countries and 1 territory), North America (23 countries and 14 territories), South America (12 countries and 2 territories), Africa (55 countries and 3 territories), and Oceania (15 countries and 19 territories)-were included in the study.

2.2 Data sources

The data sources used in this study (see Table 1) included (1) the 2010 GlobeLand30 with 30-m spatial resolution from the National High-Tech R & D Program of the Ministry of Science and Technology of China; (2) the European Space Agency climate change initiative land cover (ESA CCI LC) product with 300-m spatial resolution for 2008–2012; (3) the 2010 MODIS NDVI with 250-m spatial resolution; (4) the 2010 DMSP/OLS; (5) the 2010 USGS Landsat imagery; (6) the 2010 Google Earth imagery; and (7) other ancillary data products.

2.3 Method for mapping global ISA and UGS

Global ISA and UGS mapping included data acquisition and processing, urban land cover classification, and accuracy assessment (Figure 2). The detailed technical procedure is described as follows:

(1) Classification method. Based on the principle of hierarchical classification, this study created a new classification method for urban land-use/cover classification in two steps: first, the boundaries of built-up areas were extracted; then, the fractions of ISA and UGS within urban built-up areas were generated to analyze the distribution of ISA and UGS in different countries worldwide.

(2) Mapping the global built-up area. The built-up area was extracted from GlobeLand30 and used as a mask layer. The spatial layer was calculated to fill the land cover types of forest, grassland, and water bodies within the built-up areas through the mask layer and GlobeLand30. Homogeneous polygons of land use types in the built-up area were then created at the global scale.

(3) Calculating the building density index. The MODIS NDVI products from the Northern Hemisphere region between April and October 2010 and from the Southern Hemisphere between October 2009 and April 2010 were analyzed. The maximum value product was calculated from the MODIS NDVI time series data. To match the MODIS NDVI product at a 250 m spatial resolution, the 1 km×1 km DMSP/OLS product was resampled to a cell size of 250 m× 250 m. The building density index was then calculated based on the MODIS NDVI maximum product and the resampled DMSP/OLS product. After that, the algorithm for the ISA component was extracted based on the building density index (ISA$_{pri}$) (eq. (1)) (Lu et al., 2008; Kuang et al., 2013, 2016b).

$$ISA_{pri} = \frac{(1 - NDVI_{max}) + OLS_{nor}}{(1 - OLS_{nor}) + NDVI_{max} + OLS_{nor} \times NDVI_{max}}, \quad (1)$$

where ISA$_{pri}$ is a building density index, NDVI$_{max}$ is the maximum value of the MODIS NDVI time series data, and OLS$_{nor}$ is the normalized nighttime light index (0–1).

(4) Retrieving ISA and UGS fraction from Landsat TM. The fractional ISA data (0–100%) for each pixel within the built-up areas were extracted from Landsat TM images. Because vegetation growth phenology is different in the Southern and Northern Hemispheres, the images of peak growth were selected based on the location of the built-up areas. After radiometric calibration, atmospheric correction and geo-correction, the vegetation-impervious surface area-soil (V-I-S) model was conducted to acquire the end-members of those land cover types. A fully constrained least-squares (FCLS) solution was used to obtain the fractional images, including high-reflectance object, low-reflectance object, vegetation, and waterbody fractional images (Kuang et al., 2014). The fractional ISA was created based on the sum of high-reflectance and low-reflectance fractional images. Because waterbodies have similar spectral features to ISAs in Landsat images, threshold values of the modified normalized difference water index (MNDWI) were used to exclude waterbodies. The UGS product was generated by
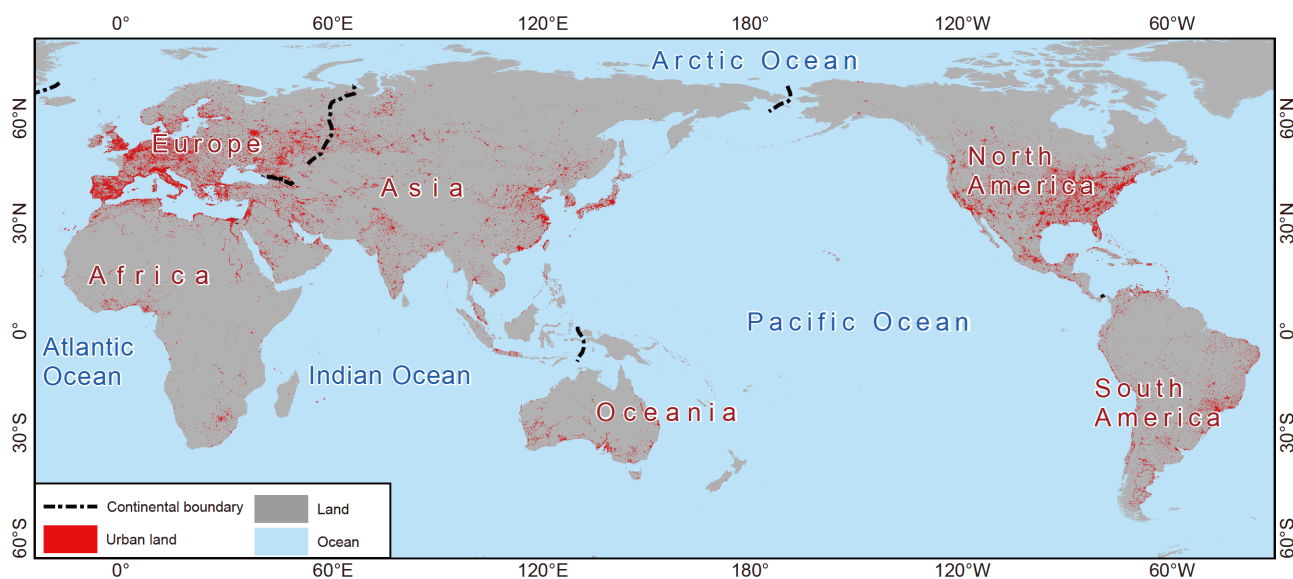
Figure 1   Spatial distribution of built-up areas at the global scale.

Table 1   Data products used in this research

Data type	Name of data source	Resolution, data type	Data source
Remotely sensed data products	GlobeLand30	30-m resolution raster data	www.globeland30.org
	MODIS NDVI	16-day 250-m composite raster data	http://modis.gsfc.nasa.gov/
	DMSP/OLS	1-km resolution raster data	http://ngdc.noaa.gov/
	ESA CCI LC	300-m resolution raster data	http://maps.elie.ucl.ac.be
	Landsat TM	30-m resolution imagery	http://glovis.usgs.gov
Supplementary data	Global administrative boundaries	Vector boundary	http://gadm.org
	1:1,000,000 global base map data	Vector boundary	National Administration of Surveying, Mapping, and Geoinformation
Dataset for accuracy assessment	Google Earth imagery	High-resolution rectified imagery	http://google-earth.en.softonic.com/
	Land use/land cover in China	30-m resolution raster data	Institute of Geographic Sciences and Natural Resources Research, Chinese Academy of Sciences
	US Geological Survey National Land Cover Database	30-m resolution raster data	http://www.mrlc.gov/nlcd2011.php

subtracting ISA, waterbody, and soil areas by using pixel calculation within built-up areas. This 30-m UGS product was used to provide the parameter calibrations for ISA and UGS data worldwide.

The advantage of FCLS spectral unmixing is that it ensures the domain value for each end-member in each pixel to be between 0 and 1, with 1 representing 100%. The specific formula is as follows:

$$R_{i\lambda} = \sum_{k=1}^{n} f_{ki} C_{k\lambda} + \varepsilon_{i\lambda}, \tag{2}$$

where $R_{i\lambda}$ is the surface reflectance of pixel i in band λ, f_{ki} is the proportion of area accounted by the component k in pixel i, $C_{k\lambda}$ is the surface reflectance of the component k in band λ, and $\varepsilon_{i\lambda}$ is the residual error value.

(5) Calibrating the parameter of the global ISA fraction. A total of 10006 samples were randomly selected from 30 cities to calibrate the parameter of the building density index (Figure 3). Based on these samples, we established a regression model (eq. (3)) to calibrate the ISA fractional images.

$$ISA_{cal} = 0.657 + 0.241 \times \ln(ISA_{pri}), \tag{3}$$

where ISA_{cal} is the postcalibration ISA index.

(6) Retrieving global ISA and UGS fractions and assessing their accuracies. By overlaying the extracted ISA fraction on the built-up area from GlobeLand30, we generated a worldwide ISA fraction map at 250 m×250 m resolution. Furthermore, a UGS fractional map was created by removing ISA fractional data in the regions of GlobeLand30's UGS pixels. The data accuracy was examined using Google Earth high-resolution images.
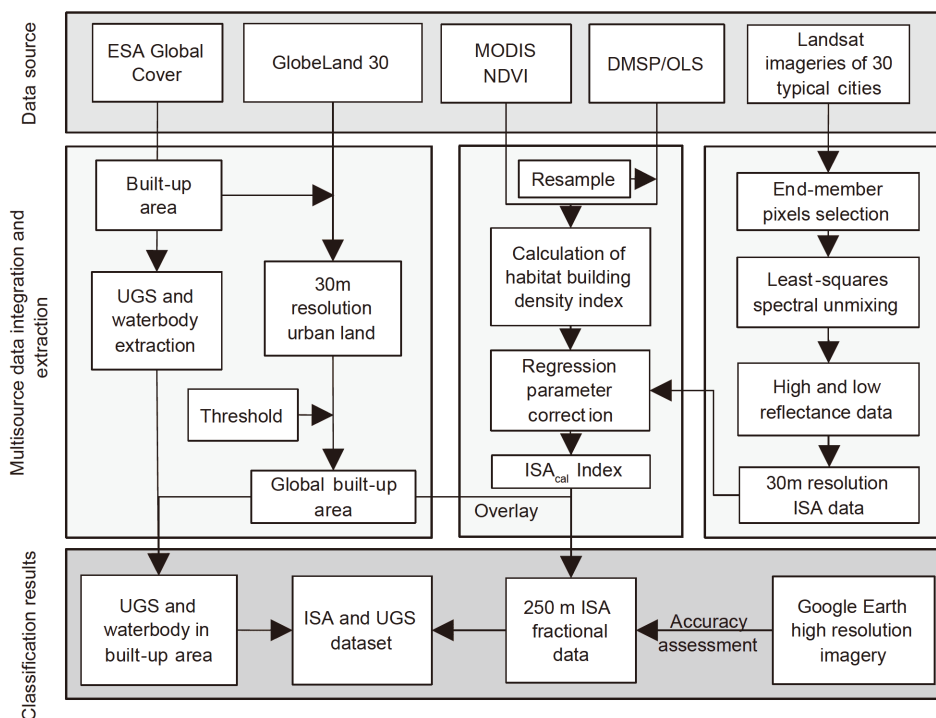
Figure 2   The framework for mapping global ISA and UGS using multiple data sources.
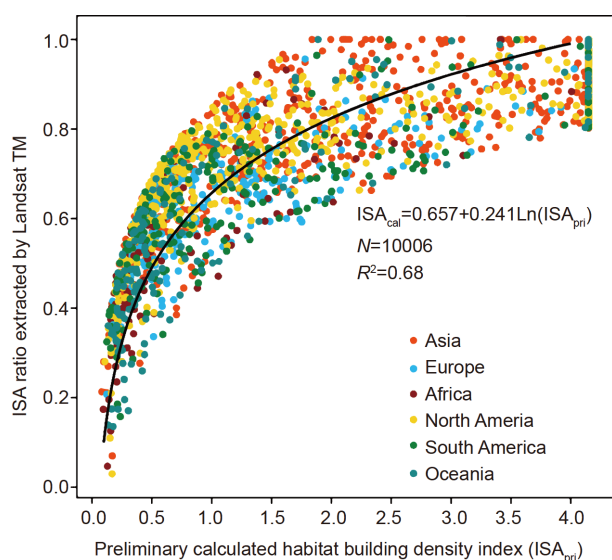

Figure 3   Regression relationship between preliminary ISA and ISA fractions extracted from Landsat TM.

(7) Spatial analysis and mapping. Specifically, we statistically analyzed the built-up area, ISA, and UGS at the continent and country scales. The fractions of ISA and UGS areas within the built-up areas were calculated at a global scale. Specific examples of each step are shown in Figure 4.

2.4   Accuracy assessment

Twenty-four typical cities were selected from different eco-

geographical zones around the world (Figure 5). These cities were mainly concentrated in global megacities such as Shanghai and London, national administrative core cities such as Moscow and Washington, and other small- or medium-sized cities. An accuracy assessment was conducted through random sampling using the 2010 Google Earth high-resolution images. To reduce the error of image registration, a 3×3 window size (750 m×750 m) was adopted for each sampling point. The fractions of ISA and UGS were interpreted visually from the Google Earth high-resolution images, representing the ground-truth value (Zhang et al., 2010). A total of 4246 samples were obtained. The mean relative error (eq. (4)) was used to evaluate the accuracy of the ISA and UGS fractions.

$$\text{MRE} = \frac{\sum_{i=1}^{n}(|x_i - y_i|/y_i)}{N}, \tag{4}$$

where MRE is the mean relative error, x_i is the ISA fraction extracted using a 3×3 window size (0–100%), y_i is the ISA from Google Earth surface verification (0–100%), and N is the number of samples.

3.   Results

3.1   Accuracy of dataset

The accuracy assessment indicated that the ISA fraction had a relatively high accuracy with a mean relative error (MRE) value of 0.19. The Asian and European cities had MRE va-
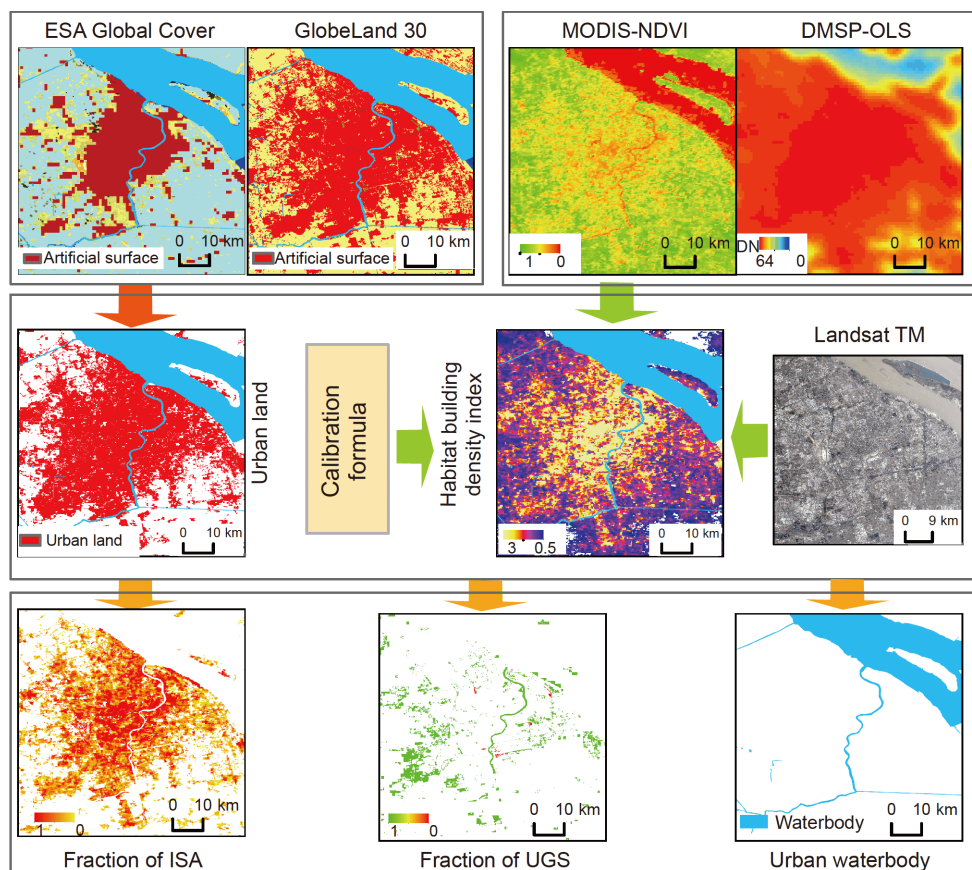
Figure 4   The specific sampling areas of the mapped global ISA and UGS in Shanghai, China.

lues of less than 0.25, Johannesburg in Africa and Brisbane in Oceania had MRE values of over 0.3, and the cities in other continents had MRE values of 0.3 or less (Figure 6). The accuracy of the ISA fraction was relatively high in cities in Asia, South America, Europe, and North America and relatively low in cities in Africa and Oceania (Figure 6). At the continental scale, the rank of MRE from the lowest to highest was as follows: Asia (MRE=0.162)<South America (MRE=0.187)<Europe (MRE=0.191)<North America (MRE=0.248)<Africa (MRE=0.308)<Oceania (MRE= 0.311). The ISA mapping accuracies were closely related to urban vegetation in the growing season and the urban planning and management levels in different countries. In regions such as Southeast Asia, Europe, and America where large cities and high vegetation coverage are common, high ISA and UGS mapping accuracies were obtained. However, the desert areas in Central Asia and Africa had relatively poor ISA mapping accuracy due to the difficulty in distinguishing ISA and UGS from other land cover types.

3.2   Spatial patterns of urban land cover

The total global urban land was 76.29×10^4 km^2 and was mainly located in North America, Europe, and Asia, ac-

counting for 86.91% of the total urban land area (66.30×10^4 km^2) (Figure 7). The top 50 countries accounted for 59.32% of the world's total urban land (Table 2), and the top 10 countries accounted for over 50% of the urban land in the top 50 countries. Of the top 10 countries, the United States ranked the highest at 15.78×10^4 km^2, followed by China (5.79×10^4 km^2), Canada (5.65×10^4 km^2), Russia (5.17×10^4 km^2), Brazil (5.11×10^4 km^2), Mexico (2.52×10^4 km^2), India (2.20×10^4 km^2), Japan (2.15×10^4 km^2), Germany (1.69×10^4 km^2), and Italy (1.57×10^4 km^2) (Figure 7).

3.3   Global patterns of ISA

The global ISA in 2010 was 45.26×10^4 km^2, accounting for 60.01% of the urban land area (Figure 8) and 0.30% of the world's land area. According to the urban ISA of each continent, the rank from the largest to the smallest was as follows: North America (15.42×10^4 km^2)>Asia (11.65×10^4 km^2)>Europe (11.06×10^4 km^2)> South America (4.30×10^4 km^2)>Africa (2.30×10^4 km^2)>Oceania (0.63×10^4 km^2). North America, Europe, and Asia accounted for 84.25% of the world's total ISA. The urban ISA was concentrated in central and southern North America (United States and
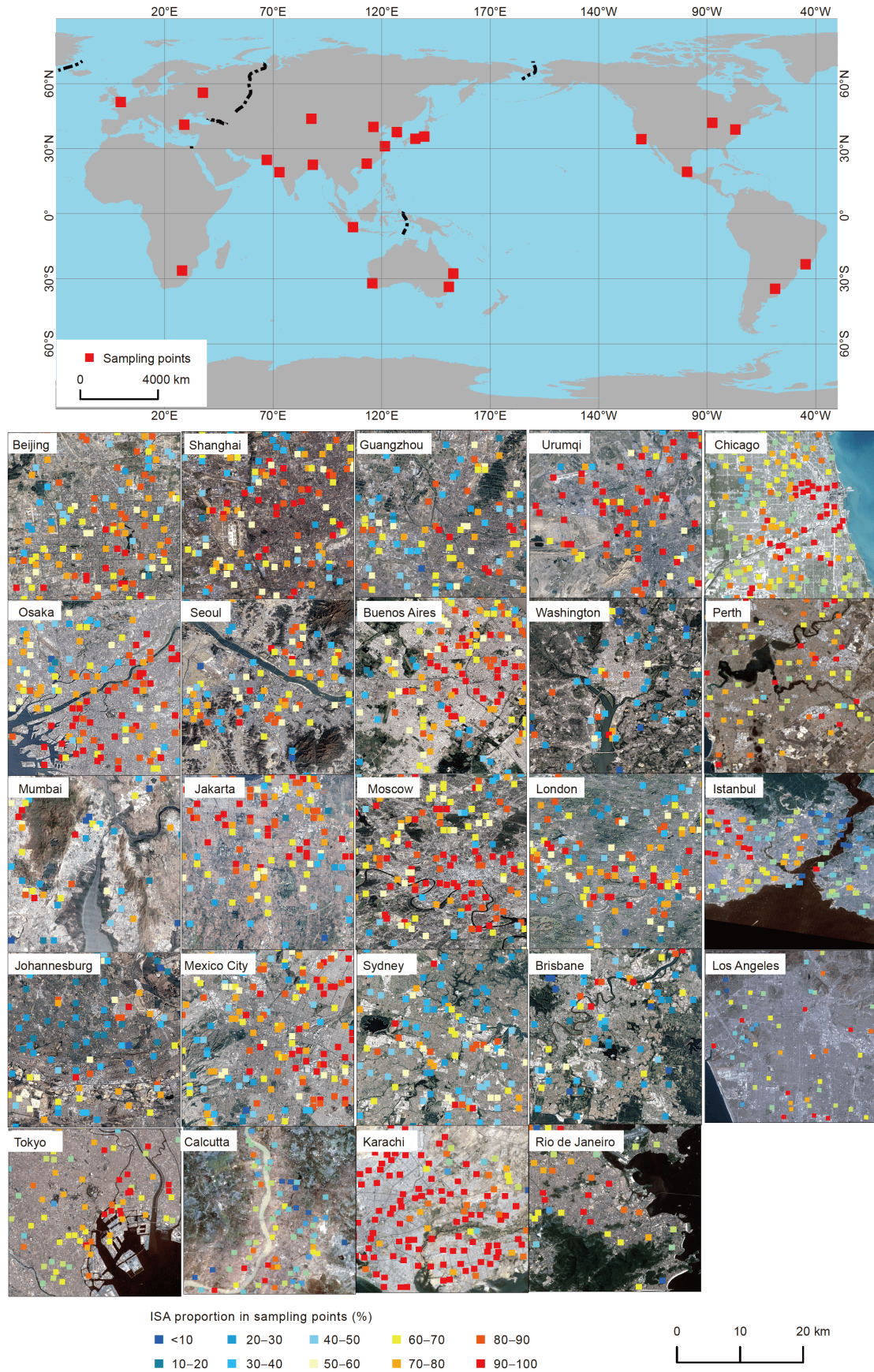
Figure 5   Spatial distribution of sampling points from specific cities for assessing ISA and UGS accuracies.
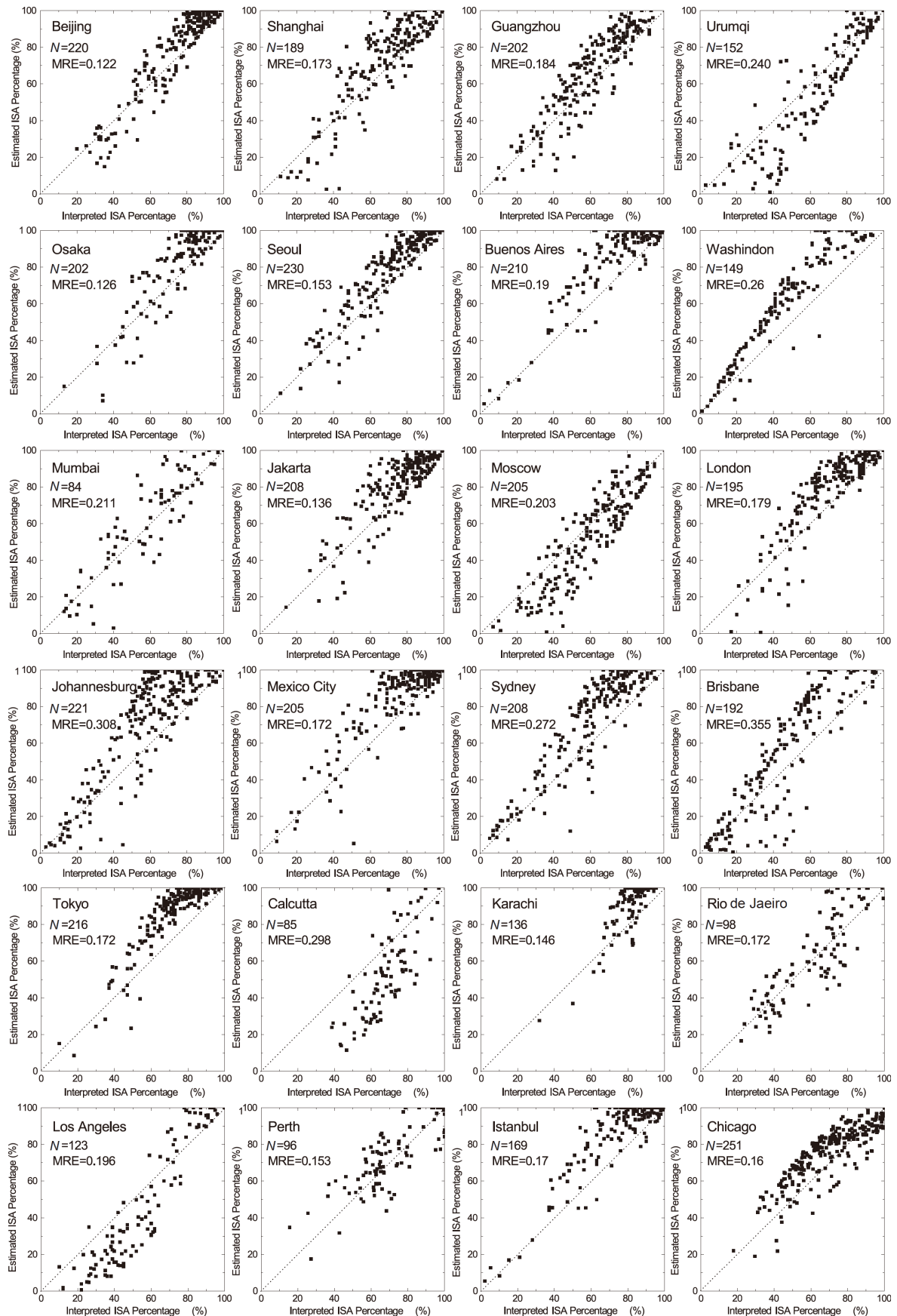
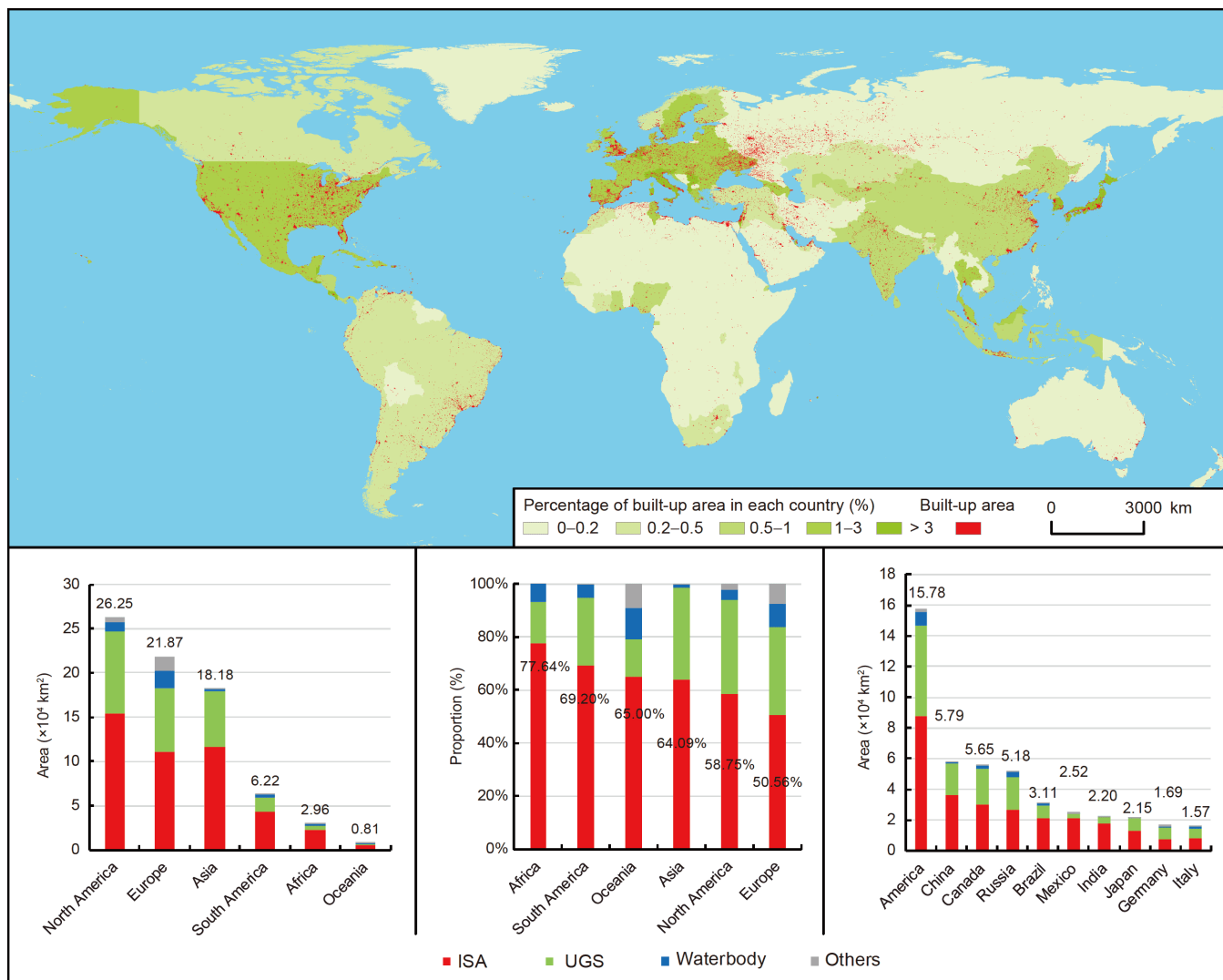**Figure 6** The accuracy of ISA fraction extraction in selected cities.

Figure 7   The proportion of urban land in each country, its total area and proportion on each continent, and the top 10 countries for ISA, UGS, waterbodies, and bare soil.

Mexico), eastern Asia (China, Japan, and Korea), Europe, and coastal regions, including the Mediterranean coast and the eastern and western coasts of the Pacific.

The ranks of ISA proportions within built-up urban areas are as follows: Africa (>70%)> South America > Oceania > Asia (>60%) > North America> Europe (>50%). Africa had the highest ISA density (77.64%), followed by South America (69.20%) and Oceania (65.00%). The proportion of ISA was closely correlated with the level of socioeconomic development and the progress of urbanization, as well as the level of urban planning and design. The three countries with the largest urban ISA were the United States, China, and Canada (8.80×10^4 km^2, 3.65×10^4 km^2, and 2.99×10^4 km^2, respectively). The top three countries with the highest ISA densities within urban areas were the African countries of Angola, Seychelles, and Comoros, with densities of 88.21%, 85.41%, and 84.71%, respectively.

3.4   Global patterns of UGS

The global UGS in 2010 was 24.92×10^4 km^2, accounting for 0.17% of the land area. The UGS areas from the largest to the smallest are North America (9.24×10^4 km^2)>Europe (7.34×10^4 km^2)>Asia (6.28×10^4 km^2)>South America (1.90×10^4 km^2)>Oceania (0.41×10^4 km^2)>Africa (0.39×10^4 km^2). The sum of UGS in North America, Europe, and Asia accounted for 89.44% of the total UGS area in the world. As shown in Figure 9, the UGS in North America was concentrated in the southeast and gradually decreased to the west, while in Asia, it was concentrated in the east and west and scattered in other regions. In South America, UGS was primarily distributed in the southeast; in both Oceania and Africa, UGS was relatively scattered. Among the world's coastal regions, the UGS was concentrated on the Mediterranean coast, the western and eastern coasts of the Pacific,

Table 2 The urban land areas of the top 50 countries and their ranks

Continent	Country	Urban area (km^2)	Rank	Continent	Country	Urban area (km^2)	Rank
North America	USA	157 785.83	1	Asia	Pakistan	5869.18	26
Asia	China	57 924.97	2	Africa	Nigeria	5224.97	27
North America	Canada	56 474.84	3	Asia	Uzbekistan	5130.83	28
Europe	Russia	51 757.06	4	Asia	Malaysia	5002.55	29
South America	Brazil	31 052.65	5	Africa	South Africa	4948.97	30
North America	Mexico	25 219.29	6	South America	Peru	4507.24	31
Asia	India	22 045.93	7	South America	Chile	4334.79	32
Asia	Japan	21 496.52	8	Asia	Iran	3626.25	33
Europe	Germany	16 865.73	9	Europe	Norway	3420.19	34
Europe	Italy	15 673.63	10	Europe	Greece	3167.96	35
Europe	Sweden	13 805.28	11	Asia	Turkmenistan	3104.68	36
Europe	France	13 610.25	12	Europe	Bulgaria	3082.44	37
Europe	Spain	12 819.09	13	Europe	Netherlands	3058.71	38
Europe	Ukraine	11 031.47	14	South America	Venezuela	3048.4	39
South America	Argentina	10 627.75	15	Europe	Czech Republic	2930.97	40
Asia	Indonesia	10 409.42	16	Africa	Tunisia	2782.62	41
Asia	Kazakhstan	10 154.68	17	South America	Columbia	2755.04	42
Europe	UK	9613.97	18	Africa	Algeria	2675.27	43
Europe	Poland	8690.16	19	Europe	Hungary	2373.56	44
Asia	Korea	8186.97	20	Asia	Turkey	2216.00	45
Europe	Serbia	7765.79	21	Europe	Belgium	2151.66	46
Europe	Romania	7122.07	22	South America	Bolivia	2103.22	47
Europe	Belarus	6348.81	23	Asia	Vietnam	2059.77	48
Asia	Thailand	6218.06	24	North America	Cuba	1956.71	49
Europe	Finland	6104.99	25	Asia	Kyrgyzstan	1885.24	50

and the western coast of the Atlantic. The proportions of UGS from highest to lowest are North America>Asia>Europe(>30%)>South America (>20%)>Africa>Oceania (>10%). North America had the highest UGS density (35.16%), followed by Asia (34.55%) and Europe (33.09%). Europe, North America, and Asia had not only relatively large UGS areas but also high UGS density within their urban areas. The results indicated that the three countries with the largest UGS areas were the United States, Canada, and Russia (5.89×10^4 km^2, 2.38×10^4 km^2, and 2.69×10^4 km^2, respectively), and the three countries with the highest UGS density were Yemen, Oman, and East Timor (58.04%, 56.07%, and 54.27%, respectively).

3.5 Landscape configurations of the urban environments in each country

In terms of ISA and UGS (Figure 10), different countries had distinct landscape configurations. For example, the proportions of ISA and UGS in Asia were 64.09% and 34.56%, respectively. Pakistan had the highest proportion of ISA

(83.15%), and Yemen had the lowest (40.19%). The proportions of ISA and UGS in Europe were 50.98% and 38.72%, respectively. Malta had the highest proportion of ISA (61.12%), and the Netherlands had the lowest (31.88%). The proportions of ISA and UGS in North America were 58.30% and 35.46%, respectively. Mexico had the highest proportion of ISA (84.37%), and Guatemala had the lowest (44.39%). The proportions of ISA and UGS in South America were 69.20% and 25.58%, respectively. Chile had the highest proportion of ISA (80.80%), and Guyana had the lowest (65.34%). In Africa, the proportions of ISA and UGS were 72.58% and 21.08%, respectively. The total urban ISA was up to 22300 km^2. Angola had the highest proportion of ISA (88.21%), and Côte d'Ivoire had the lowest (45.99%). In Oceania, the proportions of ISA and UGS were 65.00% and 14.07%, respectively. New Zealand had the highest proportion of ISA (87.29%), and Papua New Guinea had the lowest (59.59%).

The ISA and UGS proportions and landscape structures were different among continents (Figure 10). The developed countries such as the United States, the United Kingdom, and France placed emphasis on urban landscape design, espe-
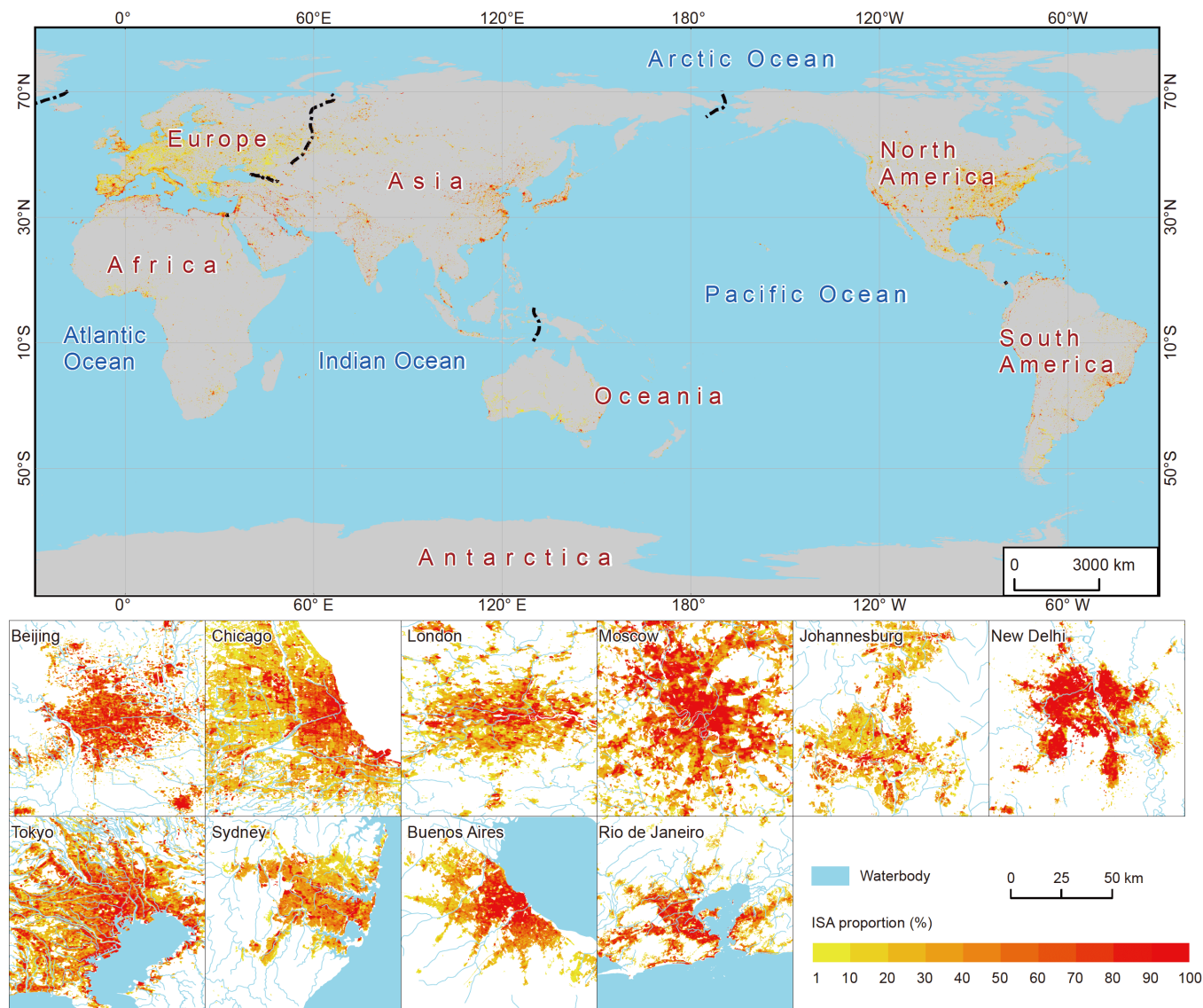
Figure 8   Global pattern of ISA and specific cases in selected cities.

cially the configuration of buildings and UGS in residential areas. Thus, the proportions of ISA within the built-up areas of these countries were relatively low, and the proportions of UGS were relatively high, indicating high-quality urban environments. In contrast, countries in Asia such as India, Mongolia, and Kazakhstan and countries in South America and Africa had relatively high ISA densities and relatively low UGS proportions, implying their relatively poor living environments (Figure 10).

The landscape patterns of ISA and UGS in the megacities on each continent were further examined. The ISA proportions can be grouped into three layout modes. Low-density and scattered distribution cities, such as Paris, Washington, D.C., and New York, belong to the category of cities with good living environments. Medium-density, clustering and filling expansion cities, such as Beijing, Moscow, and Tokyo,

where ISA extends outward from the city center with a decrease in the ISA density from the center to the outskirts. In contrast, the vegetation density gradually increases in the built-up area and enhances the urban living environments in these medium-density cities. Finally, high-density and compact cities such as Cairo, São Paulo, and New Delhi have high ISA densities and very little natural vegetation coverage. The environments in these cities are in need of improvement. The urban environments in developed countries have been significantly improved by effectively mosaicking buildings and UGS through the scientific design of urban landscapes. Meanwhile, in less developed and developing countries, the proportions of ISA with buildings, roads, and public squares are relatively high. These countries need to optimize landscape configurations and improve their urban environments.
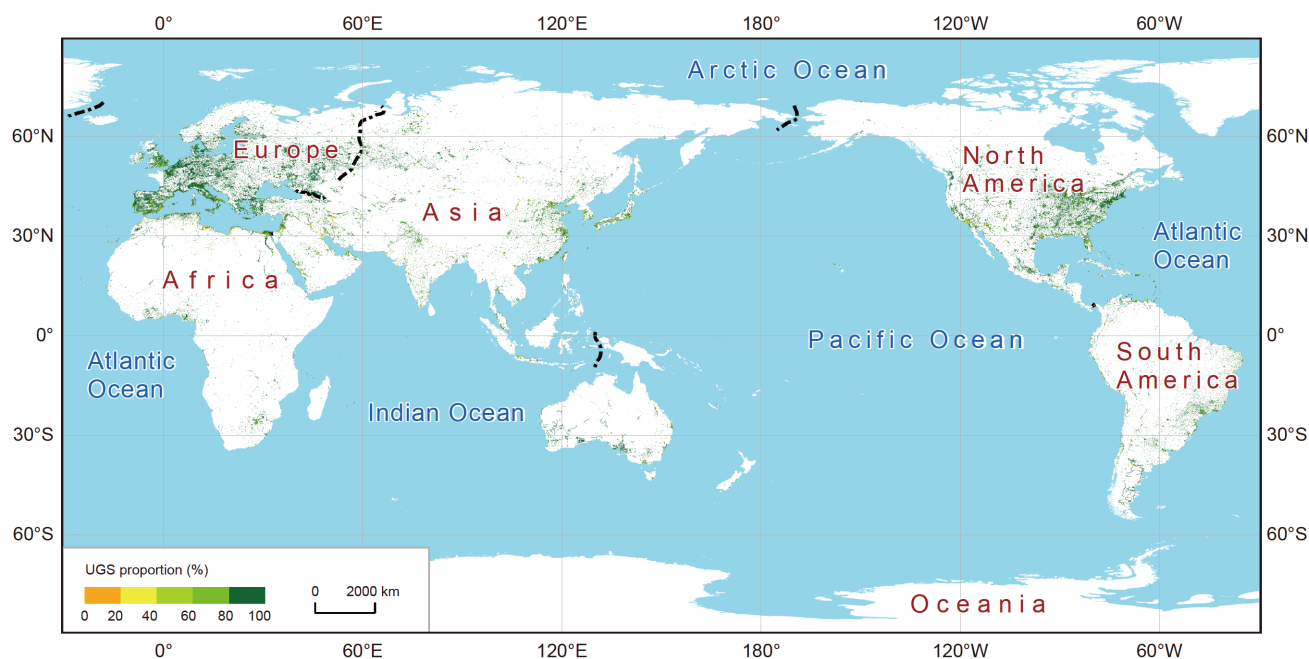
Figure 9   Global pattern of UGS.

4. Discussion

4.1 Mapping of global ISA and UGS and their potential applications to the assessment of global climate and ecological impacts

This research accurately delineated the ISA and UGS components in built-up areas using a hierarchical classification approach. We found that the classification of ISA and UGS is difficult in arid and semiarid zones using only MODIS data. DMSP/OLS data were very helpful in identifying ISA in non-vegetation areas. In addition, we found that combining multisource data (e.g., GlobeLand30 data, MODIS, DMSP/OLS) can effectively improve the global ISA and UGS mapping accuracies.

The global urban land area was estimated to be 76.29×10^4 km^2 in 2010, accounting for 0.51% of the global land area. This finding was similar to the results of Schneider et al. (2009, 2010), who showed that the global urban footprint was slightly less than 0.5% in 2001/2002, but lower than the results from Liu et al. (2018), who indicated a ratio of 0.63% in 2010. Due to the decomposition of ISA and UGS components within cities, the global ISA was assessed as 45.26×10^4 km^2, accounting for 0.30% of the global land area, which is lower than the results by Elvidge et al. (2007), who found that the proportion of constructed ISA was 0.43% in 2000/2001.

Our results indicated that the global UGS had a total area of 24.92×10^4 km^2, accounting for 0.17% of the global land area. UGS plays an important role in improving urban ecosystem services and regulating urban climate (Tigges et al.,

2013). The global ISA and UGS data developed by this study can provide important land surface parameters for global climate models. In addition, information about the fractions of ISA and UGS can be used to constrain process-based ecosystem models for quantitatively evaluating the impact of urbanization on ecological processes (Ding, 2018). Consequently, the study of accurately mapping ISA and UGS has broad prospects and potential applications in the assessment of both the global climate and the ecological impacts induced by urbanization (Ürge-Vorsatz et al., 2018).

4.2 Differences in habitat environments among developed, developing, and underdeveloped countries

Our research indicated that ISA and UGS components in built-up areas varied among developed, developing, and underdeveloped countries, implying that the differences in national planning standards among countries at different socioeconomic levels could result in significant differences in urban green infrastructure. The differences in the quality of urban environments between countries are remarkable.

The developed countries have relatively low proportions of ISA in cities. For example, the percentages of ISA and UGS were 58.40% and 35.46% in North American cities and 50.98% and 38.72% in European cities (Figures 10 and 11). The low percentages of ISA played an important role in improving urban ecosystem services by optimizing urban landscape structures (Cao et al., 2017). Developing countries have relatively high percentages of ISA in built-up areas. For example, the proportions of ISA and UGS in India (Asia)
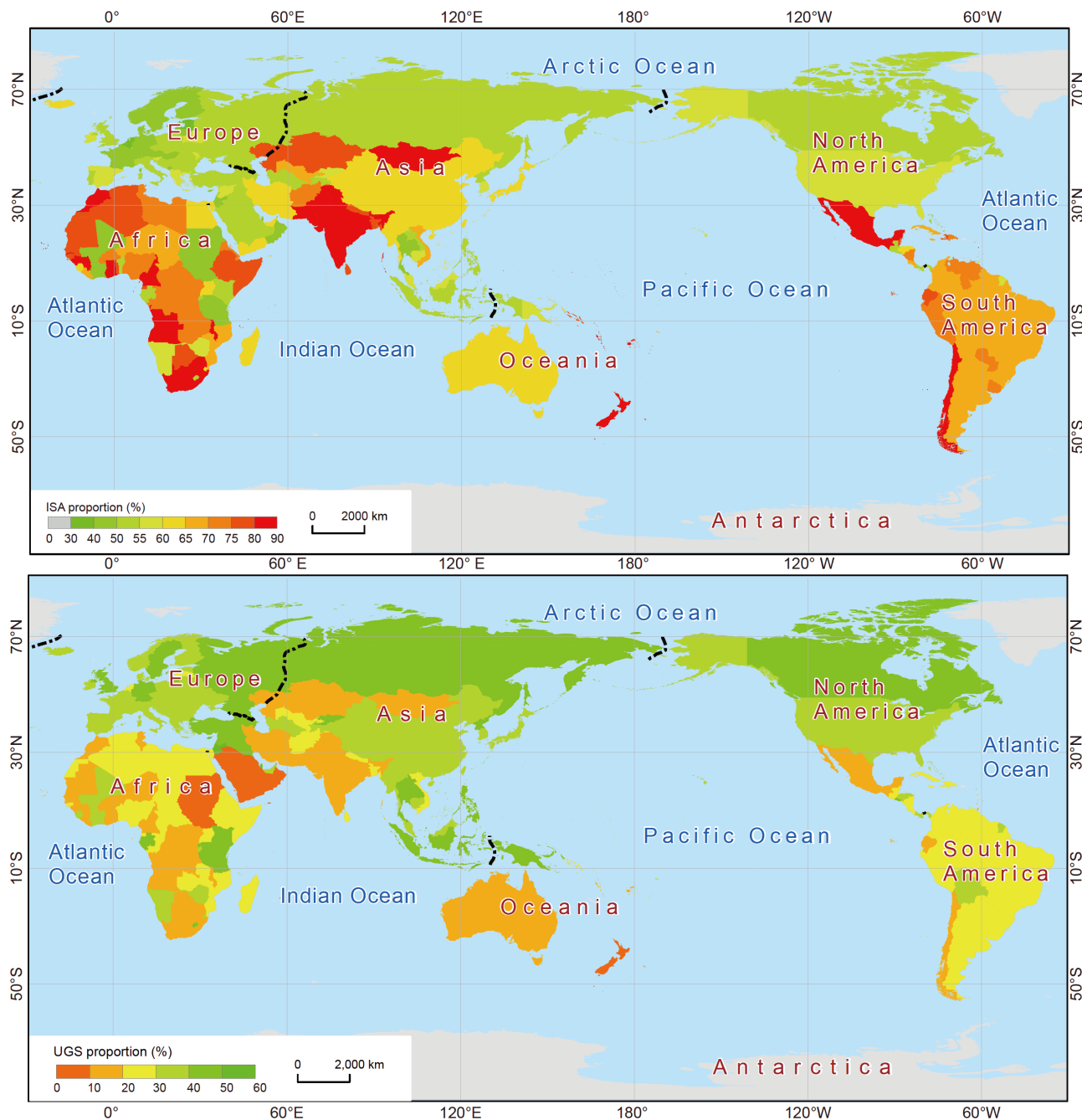
Figure 10   Distribution of the proportions of ISA and UGS in each country.

were 81.41% and 17.33%, respectively. The ecological function of UGS was relatively low, and the urban environment needs to be improved in these cities. In some underdeveloped countries, the proportions of ISA are high, while the proportions of UGS are very low in these countries. Angola had the highest proportion of ISA (88.21% of built-up area) and a very low proportion of UGS. Some African countries such as Sudan (Figure 8) had low ISA proportions as well as extremely low UGS proportions.

4.3   Implications for urban planning

High densities of ISA induced by fast urban clustering and filling expansion will increase the risk of extreme summer heat waves or storm floods in urban agglomerations. Solutions to this problem are important for designing a beautiful China and building harmonious and livable cities in a new era (Ding, 2018). The average proportion of ISA in China's built-up area is 67%. Some megacities and urban agglomerations have high densities of ISA with percentages greater
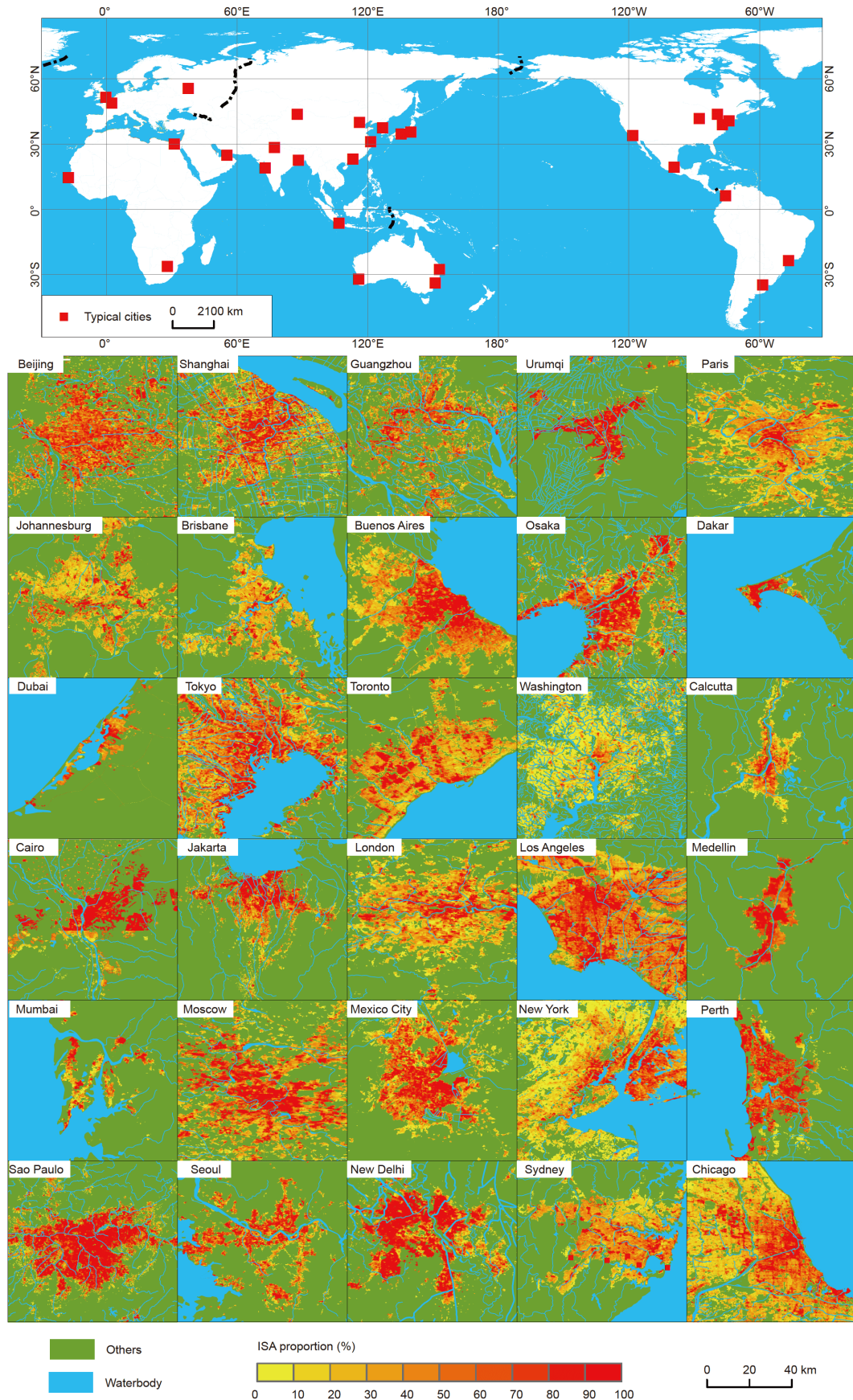
Figure 11   Distribution of ISA and UGS in typical cities.

than 80%; for example, the Beijing-Tianjin-Hebei and Yangtze River Delta urban agglomerations have ISAs of over 1000 km^2 each (Wang et al., 2012).

We found that the residential, commercial, industrial and other functional zones were mosaicked in the megacities of China. For example, the average ISA percentages in residential and commercial zones were approximately 60% and 70% in Beijing and Shanghai, respectively. The difference between commercial and residential zones is obvious in American cities such as New York and Chicago, where the ISA proportions in commercial zones and residential zones are 60–70% and 45–55%, respectively (Kuang et al., 2014; Chaudhuri et al., 2017). The proportion of ISA in urban agglomerations is obviously high as a result of the low permeability in built-up areas. We emphasize the need to control an "ecological redline" in administrative departments to avoid high-density ISA expansion. The "ecological redline" control of built-up areas in megacities and the construction of ecological patches and corridors within and between cities in urban agglomerations need to be strengthened to prevent urban filling and clustering expansion (Wu, 2018).

In view of the high proportion of ISA in developing and underdeveloped countries, we recommend that these countries take effective measures to appropriately strengthen the construction of urban green infrastructure and to improve water permeability and thermal comfort for urban dwellers (William et al., 2018). These countries should constrain city sizes and reduce ISA proportions in megacities and urban agglomerations to improve the functions of urban ecosystem services and urban environments. The proportion of ISA should be strictly controlled within 25% in the sub-basins of urban agglomerations.

5. Conclusion

This study developed the first high-precision dataset on global ISA and UGS fractions. Our estimates indicated that the total area of the world's urban land was 76.29×10^4 km^2, which was primarily distributed in central Europe, eastern Asia, and central and eastern North America. The top 50 countries accounted for 59.32% of the world's urban land, with the top three countries being the United States (urban land: 15.78×10^4 km^2), China (urban land: 5.79×10^4 km^2), and Canada (urban land: 5.65×10^4 km^2).

The total ISA in the world was 45.26×10^4 km^2, accounting for 60.01% of the urban land worldwide, and these areas were mainly distributed in central and southern North America, eastern Asia, and most regions of Europe, as well as coastal regions around the world. On the continental scale, North America, Europe, and Asia accounted for 84.25% of the ISA in the world. The fractional urban ISA on the con-

tinental scale followed the order of Africa (>70%) > South America > Oceania > Asia (>60%)> North America > Europe (>50%). Europe, North America, and Asia had relatively large ISAs in their urban areas, but the fractions of ISAs were low. Meanwhile, the UGS area followed the order of North America (9.24×10^4 km^2) > Europe (7.34×10^4 km^2) > Asia (6.28×10^4 km^2) > South America (1.90×10^4 km^2) > Oceania (0.41×10^4 km^2) > Africa (0.39×10^4 km^2). UGS was concentrated in southeastern North America, southwestern Europe, and eastern and western Asia. North America, Europe, and Asia accounted for 89.44% of the total UGS in the world.

References

Bierwagen B G, Theobald D M, Pyke C R, Choate A, Groth P, Thomas J V, Morefield P. 2010. National housing and impervious surface scenarios for integrated climate impact assessments. Proc Natl Acad Sci USA, 107: 20887–20892

Cao S S, Hu D Y, Zhao W J, Chen S S, Cheng Q W. 2017. Spatial structure comparison of urban agglomerations between China and USA in a perspective of impervious surface coverage: A case study of Beijing-Tianjin-Hebei and Boswash (in Chinese). Acta Geogr Sin, 72: 1017–1031

Chaudhuri A S, Singh P, Rai S C. 2017. Assessment of impervious surface growth in urban environment through remote sensing estimates. Environ Earth Sci, 76: 541

Chen J, Chen J, Liao A P, Cao X, Chen L J, Chen X H, He C Y, Han G, Peng S, Lu M, Zhang W W, Tong X H, Mills J. 2015. Global land cover mapping at 30 m resolution: A POK-based operational approach. ISPRS-J Photogramm Remote Sens, 103: 7–27

Chen L D, Zhou W Q, Han L J, Sun R H. 2016. Developing key technologies for establishing ecological security patterns at the Beijing-Tianjin-Hebei urban megaregion (in Chinese). Acta Ecol Sin, 36: 7125–7129

Chi W F, Shi W J, Kuang W H. 2015. Spatio-temporal characteristics of intra-urban land cover in the cities of China and USA from 1978 to 2010. J Geogr Sci, 25: 3–18

Creutzig F, Agoston P, Minx J C, Canadell J G, Andrew R M, Quéré C L, Peters G P, Sharifi A, Yamagata Y, Dhakal S. 2016. Urban infrastructure choices structure climate solutions. Nat Clim Change, 6: 1054–1056

Ding Y H. 2018. Impact of climate change and urbanization on extreme rainstorm in China's megacities (in Chinese). China Flood Drought Manage, 28: 1–2

Elvidge C D, Keith D M, Tuttle B T, Baugh K E. 2010. Spectral identification of lighting type and character. Sensors, 10: 3961–3988

Elvidge C D, Tuttle B T, Sutton P C, Baugh K E, Howard A T, Milesi C, Bhaduri B, Nemani R. 2007. Global distribution and density of constructed impervious surfaces. Sensors, 7: 1962–1979

Fang C L, Yang J Y, Kuang W H. 2017. Basic schemes and suggestions of

multi-planning integration in progress of Xiongan New Area planning (in Chinese). Bull Chin Acad Sci, 32: 1192–1198

Georgescu M, Morefield P E, Bierwagen B G, Weaver C P. 2014. Urban adaptation can roll back warming of emerging megapolitan regions. Proc Natl Acad Sci USA, 111: 2909–2914

Georgescu M, Moustaoui M, Mahalov A, Dudhia J. 2013. Summer-time climate impacts of projected megapolitan expansion in Arizona. Nat Clim Change, 3: 37–41

Grimm N B, Faeth S H, Golubiewski N E, Redman C L, Wu J, Bai X, Briggs J M. 2008. Global change and the ecology of cities. Science, 319: 756–760

Homer C H, Fry J A, Barnes C A. 2012. The national land cover database. USGS Fact Sheet, 3020: 1–4

Jones B, O'Neill B C, McDaniel L, McGinnis S, Mearns L O, Tebaldi C. 2015. Future population exposure to US heat extremes. Nat Clim Change, 5: 652–655

Kuang W H, Chen L J, Liu J Y, Xiang W N, Chi W F, Lu D S, Yang T R, Pan T, Liu A L. 2016a. Remote sensing-based artificial surface cover classification in Asia and spatial pattern analysis. Sci China Earth Sci, 59: 1720–1737

Kuang W H, Chi W F, Lu D S, Dou Y Y. 2014. A comparative analysis of megacity expansions in China and the U.S.: Patterns, rates and driving forces. Landscape Urban Plan, 132: 121–135

Kuang W H, Liu J Y, Dong J W, Chi W F, Zhang C. 2016b. The rapid and massive urban and industrial land expansions in China between 1990 and 2010: A CLUD-based analysis of their trajectories, patterns, and drivers. Landscape Urban Plan, 145: 21–33

Kuang W H, Liu J Y, Zhang Z X, Lu D S, Xiang B. 2013. Spatiotemporal dynamics of impervious surface areas across China during the early 21st century. Chin Sci Bull, 58: 1691–1701

Lee C, Kim K, Lee H. 2018. GIS based optimal impervious surface map generation using various spatial data for urban nonpoint source management. J Environ Manage, 206: 587–601

Li L W, Lu D S, Kuang W H. 2016. Examining urban impervious surface distribution and its dynamic change in Hangzhou metropolis. Remote Sens, 8: 265

Liu X P, Hu G H, Chen Y M, Li X, Xu X C, Li S Y, Pei F S, Wang S J. 2018. High-resolution multi-temporal mapping of global urban land using Landsat images based on the Google Earth Engine Platform. Remote Sens Environ, 209: 227–239

Liu Z F, He C Y, Zhou Y Y, Wu J G. 2014. How much of the world's land has been urbanized, really? A hierarchical framework for avoiding confusion. Landscape Ecol, 29: 763–771

Lu D S, Hetrick S, Moran E. 2011. Impervious surface mapping with Quickbird imagery. Int J Remote Sens, 32: 2519–2533

Lu D S, Tian H Q, Zhou G M. 2008. Regional mapping of human settlements in southeastern China with multisensor remotely sensed data. Remote Sens Environ, 112: 3668–3679

Lu D S, Weng Q H. 2006. Use of impervious surface in urban land-use classification. Remote Sens Environ, 102: 146–160

Pan J H, Li X X, Liu C Y. 2009. Urban impervious surface abundance estimation in Lanzhou City based on remote sensing (in Chinese). J Northwest Nor Univ-Nat Sci, 45: 95–100

Ridd M K. 1995. Exploring a V-I-S (vegetation-impervious surface-soil) model for urban ecosystem analysis through remote sensing: Comparative anatomy for cities. Int J Remote Sens, 16: 2165–2185

Sanchez Rodriguez R, Ürge-Vorsatz D, Barau A S. 2018. Sustainable development goals and climate change adaptation in cities. Nat Clim Change, 8: 181–183

Schneider A, Friedl M A, Potere D. 2009. A new map of global urban extent from MODIS satellite data. Environ Res Lett, 4: 044003–44011

Schneider A, Friedl M A, Potere D. 2010. Mapping global urban areas using MODIS 500-m data: New methods and datasets based on 'urban ecoregions'. Remote Sens Environ, 114: 1733–1746

Tigges J, Lakes T, Hostert P. 2013. Urban vegetation classification: Benefits of multitemporal RapidEye satellite data. Remote Sens Environ, 136: 66–75

Ürge-Vorsatz D, Rosenzweig C, Dawson R J, Rodriguez R S, Bai X M, Barau A S, Seto K C, Dhakal S. 2018. Locking in positive climate responses in cities. Nat Clim Change, 8: 174–177

Wang L, Li C C, Ying Q, Cheng X, Wang X Y, Li X Y, Hu Y Y, Liang L, Yu L, Huang H B, Gong P. 2012. China's urban expansion from 1990 to 2010 determined with satellite remote sensing (in Chinese). Chin Sci Bull, 57: 1388–1399

Wickham J D, Stehman S V, Gass L, Dewitz J, Fry J A, Wade T G. 2013. Accuracy assessment of NLCD 2006 land cover and impervious surface. Remote Sens Environ, 130: 294–304

William S, Cynthia R, Shobhakar D, Debra R, Aliyu S B, Seth S, Ürge-Vorsatz D. 2018. City transformations in a 1.5°C warmer world. Nat Clim Change, 8: 177–181

Wu C S, Murray A T. 2003. Estimating impervious surface distribution by spectral mixture analysis. Remote Sens Environ, 84: 493–505

Wu L Y. 2018. Planning and constructing healthy cities is the key to improve the livability of cities (in Chinese). Chin Sci Bull, 63: 985–985

Yang L M, Huang C G, Homer C G, Wylie B K, Coan M J. 2003. An approach for mapping large-area impervious surfaces: Synergistic use of Landsat-7 ETM+ and high spatial resolution imagery. Canadian J Remote Sens, 29: 230–240

Yu S S, Sun Z X, Guo H D, Zhao X W, Sun L, Wu M F. 2017. Monitoring and analyzing the spatial dynamics and patterns of megacities along the Maritime Silk Road (in Chinese). J Remote Sens, 21: 169–181

Yue W Z, Xu J H, Xu L H. 2006. An analysis on eco-environmental effect of urban land use based on remote sensing images: A case study of urban thermal environment and NDVI (in Chinese). Acta Ecol Sin, 26: 1450–1460

Zhang J, Zhou Y K, Li R Q, Zhou Z J, Zhang L Q, Shi Q D, Pan X L. 2010. Accuracy assessments and uncertainty analysis of spatially explicit modeling for land use/cover change and urbanization: A case in Beijing metropolitan area. Sci China Earth Sci, 53: 173–180

Zhang L, Weng Q H. 2016. Annual dynamics of impervious surface in the Pearl River Delta, China, from 1988 to 2013, using time series Landsat imagery. ISPRS-J Photogramm Remote Sens, 113: 86–96

Zhuo L, Shi Q L, Tao H Y, Zheng J, Li Q P. 2018. An improved temporal mixture analysis unmixing method for estimating impervious surface area based on MODIS and DMSP-OLS data. ISPRS-J Photogramm Remote Sens, 142: 64–77

(Responsible editor: Xin LI)